Since January 2020 Elsevier has created a COVID-19 resource centre with free information in English and Mandarin on the novel coronavirus COVID-19. The COVID-19 resource centre is hosted on Elsevier Connect, the company's public news and information website.

Biosensors and Bioelectronics 199 (2022) 113880

Contents lists available at ScienceDirect

Biosensors and Bioelectronics

journal homepage: www.elsevier.com/locate/bios

RNA polymerization actuating nucleic acid membrane (RANAM)-based biosensing for universal RNA virus detection

Dajeong Kim [1], Sangwoo Han [1], Yoonbin Ji, Heejeong Youn, Hyejin Kim, Ohsung Ko, Jong Bum Lee [*]

Department of Chemical Engineering, University of Seoul, 163 Seoulsiripdaero, Dongdaemun-gu, Seoul, South Korea

ARTICLE INFO

Keywords:
RNA-dependent RNA polymerase
Nucleic acid membrane
Nucleic acid metallization
SARS-CoV-2
RNA virus detection

ABSTRACT

The coronavirus disease (COVID-19) pandemic has shown the importance of early disease diagnosis in preventing further infection and mortality. Despite major advances in the development of highly precise and rapid detection approaches, the time-consuming process of designing a virus-specific diagnostic kit has been a limiting factor in the early management of the pandemic. Here, we propose an RNA polymerase activity-sensing strategy utilizing an RNA polymerization actuating nucleic acid membrane (RANAM) partially metallized with gold for colorimetric RNA virus detection. Following RANAM-templated amplification of newly synthesized RNA, the presence of the RNA polymerase was determined by visualization of the inhibition of an oxidation/reduction (redox) reaction between 3,3′,5,5′-tetramethylbenzidine (TMB) and blocked Au^{3+}. As a proof of concept, a viral RNA-dependent RNA polymerase (RdRP), which is found in various RNA virus-infected cells, was chosen as a target molecule. With this novel RANAM biosensor, as little as 10 min of RdRP incubation could significantly reduce the colorimetric signal. Further development into an easy-to-use prototype kit in viral infection diagnosis detected RdRP present at levels even as low as 100 aM. Color formation based on the presence of RdRP could be simply and clearly confirmed through smartphone-assisted color imaging of the prototype kit. This study provides a non-PCR-based RNA virus detection including its variants using RdRP-mediated polymerization.

1. Introduction

Since the outbreak of coronavirus disease (COVID-19), the development of rapid and reliable diagnostics for viral infections has been of great interest (Ji et al., 2020; Kevadiya et al., 2021). To date, reverse transcription-quantitative polymerase chain reaction (RT-qPCR)-based assays have been used mostly for diagnosis (Ai et al., 2020; Corman et al., 2020; Fang et al., 2020). In addition to RT-qPCR, serological and immunological assays, which detect specific antigens or antibodies in saliva or serum, have also been widely used for rapid point-of-care testing (POCT) (Carter et al., 2020; Ejazi et al., 2021; Lee et al., 2020; Song et al., 2021). However, these detection methods have a common limitation in that they require a target-specific design, which takes time to develop, resulting in a dearth of diagnostics in the early stages of a pandemic. In addition, established target-specific diagnostic kits require re-validation to determine their ability to detect newly emerging mutations (Ascoli, 2021). To minimize person-to-person transmission of contagious RNA viruses, virus species- and mutation-independent detection assays are needed which do not require any re-validation process for newly emerged viruses.

RNA-dependent RNA polymerase (RdRP), a type of replicase-transcriptase complex, is an essential catalytic protein in the RNA replication and transcription of viral genomes such as Ebola virus, Zika virus, hepatitis C virus (HCV), and coronavirus (Ahlquist, 2002; Ferrero et al., 2015; Picarazzi et al., 2020). Although RdRPs lack sequence homology, they share similar RNA-replicating functions (Ahlquist, 2002). Moreover, RdRP rapidly amplifies RNA using its backtracked-reversal replication capability (Dulin et al., 2015), enabling the detection of even small numbers of RdRP, such as those found during the early stages of an infection. Thus, RdRP is a promising and widely applicable biomarker for multiple RNA virus infection-related diseases (Aftab et al., 2020; Machitani et al., 2020; Pokhrel et al., 2020). Few studies have been conducted on RdRP detection platforms and further development of RdRP-diagnostic systems is pivotal for its practical diagnostic

* Corresponding author.
E-mail address: jblee@uos.ac.kr (J.B. Lee).
[1] These authors contributed equally.

https://doi.org/10.1016/j.bios.2021.113880
Received 24 September 2021; Received in revised form 7 December 2021; Accepted 9 December 2021
Available online 10 December 2021

application (Han et al., 2021).

Various nucleic acid-based biosensing nanodevices have been developed, providing target-recognizing sequences and an excellent signal amplification platform (Abi et al., 2018; Du and Dong, 2017; Krishnan and Simmel, 2011). In particular, nucleic acid-templated metallization offers enriched metal probes that significantly enhance the optical, chemical, and electrical signals, enabling ultrasensitive detection (Chen et al., 2018; Ma et al., 2019; Qing et al., 2019; Wu et al., 2014; Zhou et al., 2017). However, most metallization of nucleic acids has been applied to simple linear strand-based or nano-sized structures whose practical utilization for rapid POCT kits may be challenging. In particular, among nucleic acids, RNA is not often used as a metallization template due to its instability. In this reason, developing metallized RNA materials with high stability can broaden the diagnostic range by making use of the multiple beneficial functions of RNA and its biological interaction with other biomolecules. In addition, scaling up of RNA-based materials is imperative for development of practical devices. In this regard, the two-dimensional macroscopic nucleic acid membrane structure, which we recently developed, offers advantages such as ultra-stable, solid, and free-standing properties, which are suitable for practical diagnostic kits (Han et al., 2014; Kim et al., 2020).

Based on our technology for macroscopic RNA structures, here, we introduce an RNA polymerization actuating nucleic acid membrane, called RANAM, based biosensor for viral RNA polymerase detection. By deriving the automated transcription of viral RNA polymerase on nucleic acid membrane that are made up of a number of RNA strands, the existence of viral RdRP could be efficiently confirmed. With the subsequent change of surface property by the natural RNA-directed RNA amplification capability of RdRP, the significantly amplified RNA on RANAM efficiently shielded Au components on the RANAM, hindering the interaction between the Au component and TMB. This hindrance led to inhibition of the colorimetric change observed with unamplified RANAM, which rapidly turned blue. For practical applications, we designed an easy-to-use and self-operating prototype kit based on RANAM for RNA virus detection. Using this system, viral infections can be easily confirmed with the naked eye. In addition, color imaging using a smartphone can be conveniently applied for rapid and accurate confirmation of the presence of viral RdRP. Our RANAM biosensor could achieve the RdRP detection without additional enzymes and primers, and regardless of the variants. Thus, this RANAM biosensor for viral RdRP detection system provides a novel perspective on the development of a universally applicable detection kit for RNA viruses. Combining with target-specific RT-PCR or immunological methods, RdRP-based detection would have great potential to improve the specificity and rapidity by double-checking the virus infection.

2. Materials and methods

2.1. Preparation of circular DNAs

92 nt- or 87 nt-phosphorylated DNA (IDT) was mixed with 22 nt-primer DNA (IDT) (Table S1 and Table S2) in nuclease-free water at a final concentration of 10 μM. Circular DNA was prepared by annealing of linear DNA (10 μM) and primer (10 μM) mixed solution from 95 °C for 5 min and to 25 °C for 1 h with gradual cooling in a thermal cycler (Bio-Rad). The reaction solution was then mixed with T4 DNA ligase (0.03 U ml^{-1}, Promega) in 1X ligation buffer (30 mM Tris–HCl, 10 mM $MgCl_2$, 10 mM DTT, and 1 mM adenosine triphosphate) and incubated at room temperature overnight to ligate the nick in circularized DNA. To purify the circular DNA, zeba spin desalting column (Thermo Scientific) was used, and 2 U and 10 U of Exonuclease I & III was treated at 37 °C to remove non-circular DNA. Then, this solution was incubated at 80 °C for 30 min to inactivate the Exonuclease. The circular DNA (1 μg) was analyzed by 3% agarose gel electrophoresis at 80 mV for 110 min, stained by GelRed, and then imaged with a Gel Doc EZ imager (Bio-Rad).

2.2. Fabrication of nucleic acid (NA) membranes by complementary rolling circle replication (cRCR) and evaporation-induced self-assembly (EISA)

NA membranes were fabricated as previously described (Han et al., 2014; Kim et al., 2020). DNA membranes were synthesized by complementary rolling circle amplification (cRCA) using two circular DNA fragments that were partially complementary to each other (Table S1). The hybridization was carried out at room temperature for 2 h by incubating an equimolar solution of primer and circular DNA. Two circular DNA fragments at a final concentration of 0.5 μM were mixed with 2 mM deoxyribonucleotide triphosphate mix (Thermo Scientific), 1X phi 29 DNA polymerase buffer (50 mM Tris-HCl, 10 mM $(NH_4)_2SO_4$, 4 mM dithiothreitol, 10 mM $MgCl_2$, pH 7.5), and 1 U μl^{-1} phi 29 DNA polymerase (Lucigen). The reaction mixture was incubated at 30 °C for 4 h to allow cRCA, and then evaporated by leaving the tube open overnight at 30 °C.

To synthesize RNA membranes, two partially complementary circular DNA fragments bearing the T7 promoter region (Table S2) were used. For complementary rolling circle transcription (cRCT), two circular DNA fragments at a final concentration of 3 μM were incubated with 3.75 mM ribonucleotide triphosphate mix (New England Biolabs; NEB), 2X reaction buffer (60 mM Tris–HCl, 9 mM $MgCl_2$, 1.5 mM DTT, and 3 mM spermidine, pH 7.9), and 5 U μl^{-1} of T7 RNA polymerase (NEB) at 37 °C for 20 h. The tube was left open to allow EISA and the reaction mixture was then evaporated overnight at 37 °C. After EISA process, the remaining reactant was removed and washed four times with nuclease-free water.

2.3. Synthesis of RANAM by metallization of NA membranes with gold

To metallize the NA membranes, 2 mM of $HAuCl_4$ was introduced into a single NA membrane. After overnight incubation at room temperature, excess Au^{3+} were washed three times with nuclease-free water. Then, 5 mM of hydroxylamine hydrochloride (HAHC; Alfa Aesar) was added to the Au-NA membranes to de-shield and expose the NA strands on the NA membrane surfaces. After 30 min of incubation at room temperature, the resulting RANAM was washed thoroughly with nuclease-free water and stored at 4 °C until use.

2.4. Characterization of NA membranes, Au-NA membranes, and RANAMs

After fabrication, colorimetric changes in the membranes were observed using a bright-field microscope (Korea Lab Tech Corporation, KI-400). The internal structure and the generation of gold nanoseeds were examined using a transmission electron microscope (TEM; JEOL, JEM2100F) and a scanning TEM (STEM). High resolution images were obtained using a field-emission scanning electron microscope (FE-SEM; Hitachi, SU8010). The roughness of the membrane surfaces was observed using a non-contact surface profiler (Bruker, Contour GT-K), and the roughness was expressed as the root mean square (Rq) of the profile. In addition, an atomic force microscope (AFM; Park Systems, NX10) was used to visualize the surface and morphological changes in the membranes. The absorbance of NA membranes, Au-NA membranes, and RANAMs were measured at different spectra using a spectrophotometer (Thermo Scientific, Nanodrop 2000c).

2.5. RNA transcription on DNA-based RANAM (D-RANAM) using DNA-directed T7 RNA polymerase

To detect T7 polymerase activity using D-RANAM, a DNA membrane was fabricated using T7 promoter-bearing Cir 3 (Table S1) and metallized into D-RANAM. Then, a single D-RANAM was incubated with 1 mM ribonucleotide solution mix, 2X RNA polymerase reaction buffer (80 mM Tris-HCl, 12 mM $MgCl_2$, 2 mM DTT, 4 mM spermidine), 0.8 U

μl^{-1} RNase inhibitor and 0, 10, or 40 U μl^{-1} T7 RNA polymerase at 37 °C for 2 h. Colorimetric changes in D-RANAM were observed using a bright-field microscope in microscopic view.

2.6. Purification of recombinant RdRP protein from Escherichia coli

The RdRP protein was expressed and purified from *Escherichia coli* (*E. coli*), which was used as a host strain. As a first step, the bacteriophage Φ6 RdRP gene (NC_003715.1) was PCR amplified using the primers RdRP-F (5′-cttacatatgccgaggagagctcccgcgtt-3′) and RdRP-R (5′-gactctcgagcctcggcattacagaacgga-3′) and the synthesized RdRP DNA fragment (Bioneer Corp., Republic of Korea) as a template. The amplified PCR product was digested with NdeI and XhoI and ligated with the NdeI/XhoI-digested pET22b plasmid (Novagen, USA). The resulting plasmid was transformed into *E. coli* BL-21 (DE3). The *E. coli* BL-21 (DE3) strain expressing the RdRP protein was cultured in Luria-Bertani (LB) medium at 37 °C. RdRP protein expression was induced using 0.2 mM isopropyl β-D-1-thiogalactopyranoside (IPTG) at 16 °C for 20 h. The cultured samples were collected by centrifugation at 3134×*g* for 20 min. The cell pellet was resuspended in 20 ml Buffer A solution (50 mM sodium phosphate, 300 mM NaCl, 20 mM β-mercaptoethanol, 0.5 mM PMSF, 10% (v/v) glycerol, pH 7.5) containing 10 mM imidazole. The cell pellet was lysed by sonication using Vibra-Cell VCX 130 (Sonics & Materials Inc., USA), and the supernatant was collected and loaded onto a Ni^{2+}-NTA column (Invitrogen, USA, R901-15). The RdRP protein bound to the Ni^{2+}-NTA column was eluted with Buffer A solution containing 300 mM imidazole. The eluted solution was desalted by dialysis with Buffer B (50 mM HEPES, 100 mM NaCl, 20 mM β-mercaptoethanol, pH 7.5) at 4 °C overnight. The dialyzed proteins were concentrated on a centrifugal filter device (30 kDa MWCO, Millipore) and supplemented with 20% (v/v) glycerol for storage. Protein concentration was determined using the Bradford assay, with bovine serum albumin as a standard.

2.7. RNA-directed RNA transcription on RANAM by RdRP

A single RANAM was incubated with 1 mM ribonucleotide solution mix, 40 mM Tris-HCl, 0.5 mM $MgCl_2$, 2 mM $MnCl_2$, 10 mM ammonium acetate, 0.8 U μl^{-1} RNase inhibitor, and 100 aM, 100 fM, 100 pM, or 100 nM of RdRP for 2 h at 30 °C. The resulting RANAM was stained with SYBR green I to quantify RNA-directed RNA transcription on RANAM, and fluorescence images were taken using an inverted fluorescence microscope (Nikon, Eclipse TiU). To examine the surface of the RANAMs, the samples were prepared on a Si wafer and observed using FE-SEM.

2.8. Redox reaction with TMB for inducing colorimetric signal

After RANAM transcription using RdRP, excess reactants were removed and RANAM washed with fresh nuclease-free water through gentle pipetting. Then, dehydrated RANAM was incubated with TMB solution (Invitrogen) for 5 min at room temperature. Colorimetric changes in the RANAM were visualized using a digital camera (Canon, EOS M6) in macroscopic view or bright-field microscopy in microscopic view. Absorbance spectra were measured using a spectrophotometer.

2.9. Analysis of Raman spectra of RNA membrane and R-RANAMs

Initial RNA membrane, R-RANAM, and R-RANAMs after the incubation with RdRP were prepared on the Si wafer and dried. Raman spectra were measured by using SERS spectrum by a Raman spectrometer (SR-303i, Andor Technology) with 785 nm laser module I0785SR0100B1 (Innovative Photonic Solution Inc.).

2.10. Application to RdRP-detection prototype kit

The prototype kit scaffold was designed using TinkerCad and used to build a kit body (1.0 cm × 1.2 cm × 2.5 cm) with two holes for loading RANAM and the reaction mixture. The resulting scaffold was printed using a multijet 3D printer (3D Systems, ProJet 3510 HD) using biocompatible UV-curable resin (3D Systems, Visijet M3 crystal). Then, RANAMs were inserted into the control (C) and test (T) line holes of the detection kit. For the RdRP-positive sample, 10 μl precursor solution containing 100 pM RdRP was placed on the T line. For the RdRP-negative sample, the same precursor solution without RdRP was placed on the T line. The detection kit was incubated for 2 h at 30 °C. After transcription by RdRP, TMB solution was added to the C and T lines, and the membrane incubated for 5 min at room temperature. The resulting prototype kit was imaged using a digital camera and filtered with a selective color spot function (Samsung, Galaxy S21), and the entire process was represented as color imaging. The RGB digital images were further processed into HSB images using ImageJ software, and the hue image was expressed in pseudocolor. For colorimetric analysis, the saturation intensity of the C or T lines based on the color image was analyzed using ImageJ software.

3. Results and discussion

3.1. Fabrication and characterization of NA membranes, Au-NA membranes and RANAMs

The two key RANAM requirements for RNA polymerase detection are: i) NA membrane for target RNA polymerase-mediated amplification and ii) Au components for enhancing the colorimetric signal (Fig. 1). The NA membrane scaffolds were constructed using multiple repeated NA strands generated from cRCR (Fig. 1a). To synthesize the DNA membrane, complementary DNA strands were extended from circular DNA using phi 29 DNA polymerase via cRCA. Following the subsequent EISA process, double-stranded DNA (dsDNA) strands are highly entangled and concentrated, generating a two-dimensional macroscopic DNA membrane on the inner surface of the tube (Fig. 1a). Similarly, for RNA membrane, two RNA strands were repetitively and continuously transcribed by T7 RNA polymerase from two complementary circular DNA strands. These RNA strands can be hybridized into partially double-stranded RNA (dsRNA), which are ultimately self-assembled into RNA-based membranes in sequential EISA step.

The NAs provide a number of binding sites for the Au cation (Berti and Burley, 2008), leading to spatially confined enrichment of Au^{3+} by NA-templated metallization to generate Au-NA membranes (Fig. 1b). The sequential reduction process induces the seeded growth of Au nanoparticles (AuNPs) inside the NA membranes and exposes the Au-covered NA strands by gathering the Au^{3+}. Exposed NA strands can attract target RNA polymerase and serve as a template for replication of RNA transcripts that shield the RANAM surface. It is noteworthy that the newly generated RNA transcripts on the surface of NA membranes block access to the TMB substrate which can be oxidized by Au to give a blue color. Finally, an RNA-based RANAM biosensor-based prototype kit for viral RdRP was designed to expedite the practical application of our system (Fig. 1b). By simply observing the blue lines in the test kit, the presence of RdRP was rapidly confirmed with the naked eye or smartphone-assisted color imaging.

Millimeter-sized DNA membranes were successfully synthesized via self-assembly of multimeric DNA amplicons using phi 29 DNA polymerase elongated from the circularized DNAs (Fig. 2a). The circular DNAs were successfully prepared by annealing of linear and primer DNA strands followed by additional purification process (Fig. S1). Interestingly, the colorless DNA membrane shrank and exhibited a yellow color upon consecutive metallization with gold, indicating high adsorption of gold ions to DNA strands. The Au^{3+}-bound DNA membrane then changed to dark green RANAM after a partial reduction reaction.

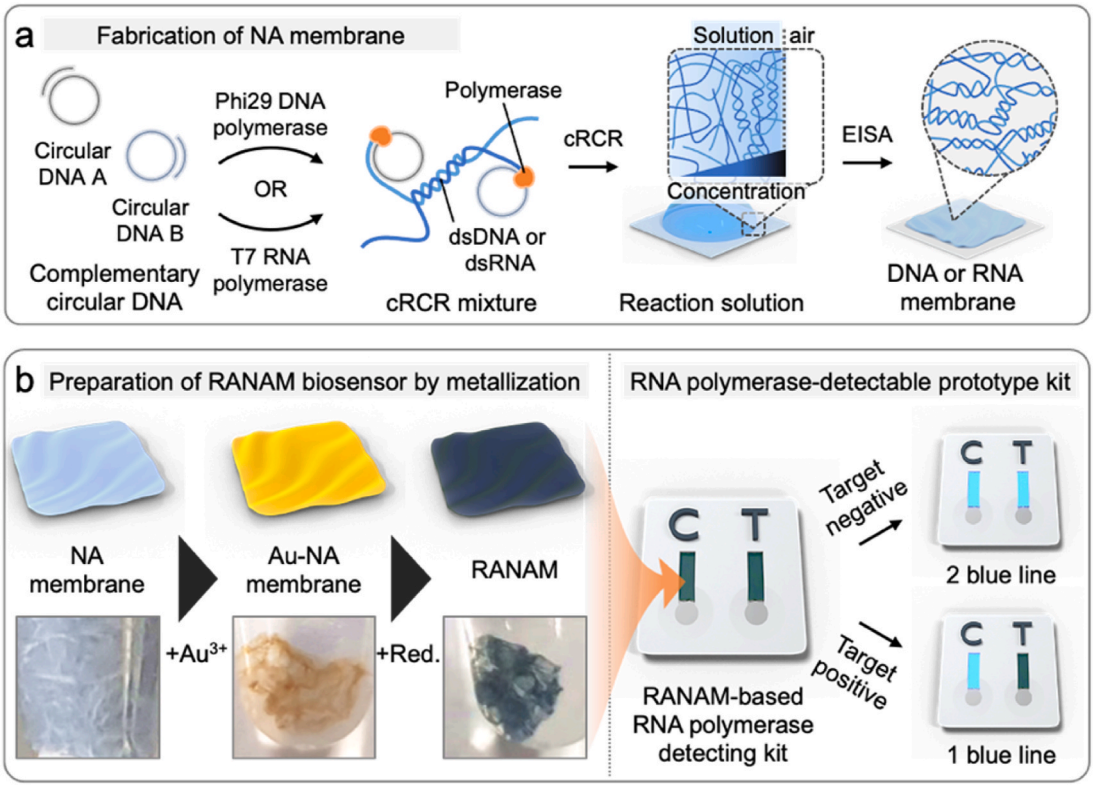

Fig. 1. Schematic illustration of the fabrication of RANAM and RANAM biosensor-mediated RNA polymerase detection. **(a)** Fabrication of NA membranes by complementary rolling circle replication (cRCR) with two complementary circular DNA strands, A and B. For the DNA membrane, multimeric DNA strands were amplified from two partially complementary circular DNA strands via complementary rolling circle amplification (cRCA) using phi 29 DNA polymerase. Similarly, tandem repeats of RNA strands were first fabricated by complementary rolling circle transcription (cRCT) with circular DNAs bearing the T7 promoter region. This was followed by an evaporation-induced self-assembly (EISA) process, the reacting cRCR solution was concentrated, and NA strands were highly entangled and self-assembled into NA membranes. **(b)** Gold metallization of NA membranes with $HAuCl_4$ to generate Au-NA membranes fully covered with Au^{3+}. Sequential reduction (Red) allowed the partial exposure of NA strands to fabricate RANAM, enabling recognition by RNA polymerase. RANAM was further utilized for the development of a kit for detection of target RNA polymerase such as RdRP. In the presence of target RNA polymerase, the NA templates can be amplified to generate new RNA transcripts, blocking the surface of RANAM, and inhibiting the redox reaction with the TMB substrate. (For interpretation of the references to color in this figure legend, the reader is referred to the Web version of this article.)

Further examination using transmission electron microscope (TEM) demonstrated that the membrane was densely packed with DNA strands in which several sub-nanometer spherical nanoparticles were generated and distributed sparsely after gold metallization (Fig. 2a). These relatively small spherical nanoparticles exhibited high electron density and were assumed to be Au nanoclusters, which would be reduced by nucleotides (Fig. S2a) (Chen et al., 2018; Kunoh et al., 2018; Lee et al., 2021). As expected, subsequent reduction accelerated the growth of larger AuNPs, up to 100 nm, by gathering and agglomerating Au nanoseeds and Au^{3+} (Fig. S2b). In addition, contact surface profiler-based analysis showed that the rough surface of the DNA membrane was mitigated (Fig. 2b). Compared to the naked DNA membrane embedded with grain-like spherical sponges with a rough surface, the Au-DNA membrane exhibited a thin, flattened, and porous morphology after gold metallization (Fig. 2c). The Au^{3+} cation gradually coat the DNA membrane, inducing the morphological flattening of the surface (Fig. S3). In addition, the complexation into DNA-Au^{3+} would reduce the repulsive interactions of anionic DNA strands, inducing the shrinkage of the densely packed DNA membrane (Chen et al., 2018; Che et al., 2015; Zinchenko et al., 2016). Moreover, Z-height images observed using AFM showed that Au^{3+} induced a 2-fold decrease in thickness, likely due to the electrostatic and coordination interaction-mediated contraction between NA and Au^{3+} (Fig. S4). Despite of the morphological changes, the membrane maintained its integrity during the Au^{3+} treatment process without any observable dissolution of DNA strands, demonstrating its rigidity and stability (Fig. S5). Moreover, the image of membrane reveals the size of millimeter-scale horizontal and vertical dimension (Fig. S6). Both of DNA membrane and Au-DNA membrane could be observed by naked eye.

As we expected, the RNA membrane was also successfully covered with Au^{3+} to form an Au-RNA membrane, as the DNA membrane and was successively reduced to generate dark-green RNA-based RANAM (Fig. 2d). It should be noted that the Au-RNA membrane and R-RANAM displayed rigid mechanical properties strong enough to enable them to be freestanding in the air (Fig. 2e). The data suggested that the NA membranes could adsorb the Au^{3+} efficiently and become enriched with metallic probes, regardless of the NA species, while preserving the filmy, ultra-stable, and free-standing structure. Moreover, these results indicate that Au^{3+} existed primarily as NA-bound ions or as nanoclusters following NA-templated reduction, which then acted as both nanoseeds and ingredients for further seeded plating into AuNPs at the reduction step with de-shielding the NA strands.

3.2. *Gold-mediated colorimetric signal amplification and its inhibition via RANAM-templated RNA transcription using T7 RNA polymerase*

Based on the localized Au^{3+} and AuNPs on the Au-embedded membranes, Au-mediated redox reactions can be initiated on the membrane structures. With the introduction of TMB, both the Au-DNA membrane and D-RANAM were colored blue regardless of the additional reduction step (Fig. 3a) (Xia et al., 2015). On the basis of a simple redox reaction

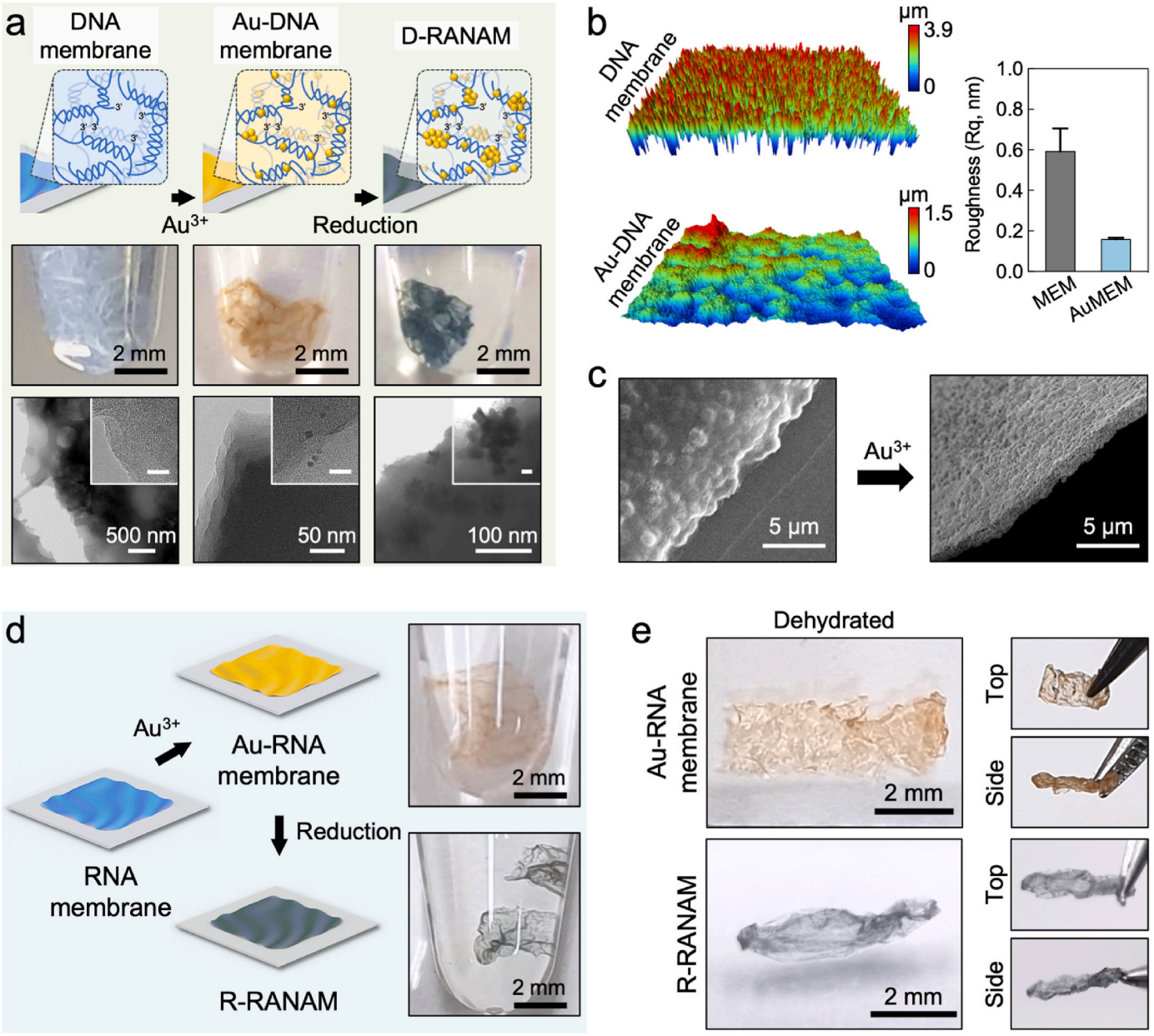

Fig. 2. Fabrication and characterization of NA membranes, Au-NA membranes, and RANAMs. **(a)** Digital and TEM images of DNA membrane, Au-DNA membrane, and D-RANAMs indicating successful metallization with gold and subsequent reduction into a dark-green color with growth of internal AuNPs. Inset scale bars represent 10 nm. **(b)** 3D-constructed non-contact surface profiler images and roughness of DNA and Au-DNA membranes. The dimensions of the images are 130 μm × 95 μm. **(c)** FE-SEM images of DNA and Au-DNA membranes showing morphological changes after metallization. (**d**) Synthetic drawing and digital images of yellow Au-RNA membrane and dark-green R-RANAM in solution. **(e)** Free-standing and rigid mechanical properties of Au-RNA membrane and R-RANAMs after dehydration. (For interpretation of the references to color in this figure legend, the reader is referred to the Web version of this article.)

between TMB and the Au component, TMB reacted rapidly and continuously on the membrane, inducing a gradual color change from yellow to blue that was clearly observable with the naked eye (Fig. 3b). Further analysis of absorbance showed enhanced absorbance at approximately 670 nm, the specific peak of oxidized TMB (oxTMB), proving successful conversion of TMB into oxTMB by Au^{3+} and AuNP, and its high deposition on the Au-DNA membrane (Fig. 3c) (Li et al., 2019; Chen et al., 2020; Wang et al., 2014; Zuber et al., 2016).

It is worth noting that the additional RNA transcription on RANAM could change the degree of redox reactions between RANAM and TMB. With the highly concentrated NA template for RNA polymerase, D-RANAM can serve as an outstanding template for T7 RNA polymerase-induced RNA transcription. To analyze the controllability of redox reaction, DNA-directed T7 RNA polymerase was used to treat D-RANAM, which bears the T7 promoter region (Fig. 3d). Interestingly, D-RANAM-templated RNA transcription significantly decreased the redox reaction between D-RANAM and TMB, inhibiting the blue color change. This result suggests that the RNA polymerase amplifies the RNA strands on the D-RANAM, blocking Au^{3+} and AuNP from reacting with TMB. Taken together, the RANAM platform has great potential as a biosensor for detecting RNA polymerases based on simple observation of coloration of macroscopic RANAMs with the naked eye.

3.3. Viral RdRP detection using the RANAM biosensor

Based on the RNA polymerase-dependent coloration, viral RdRP was

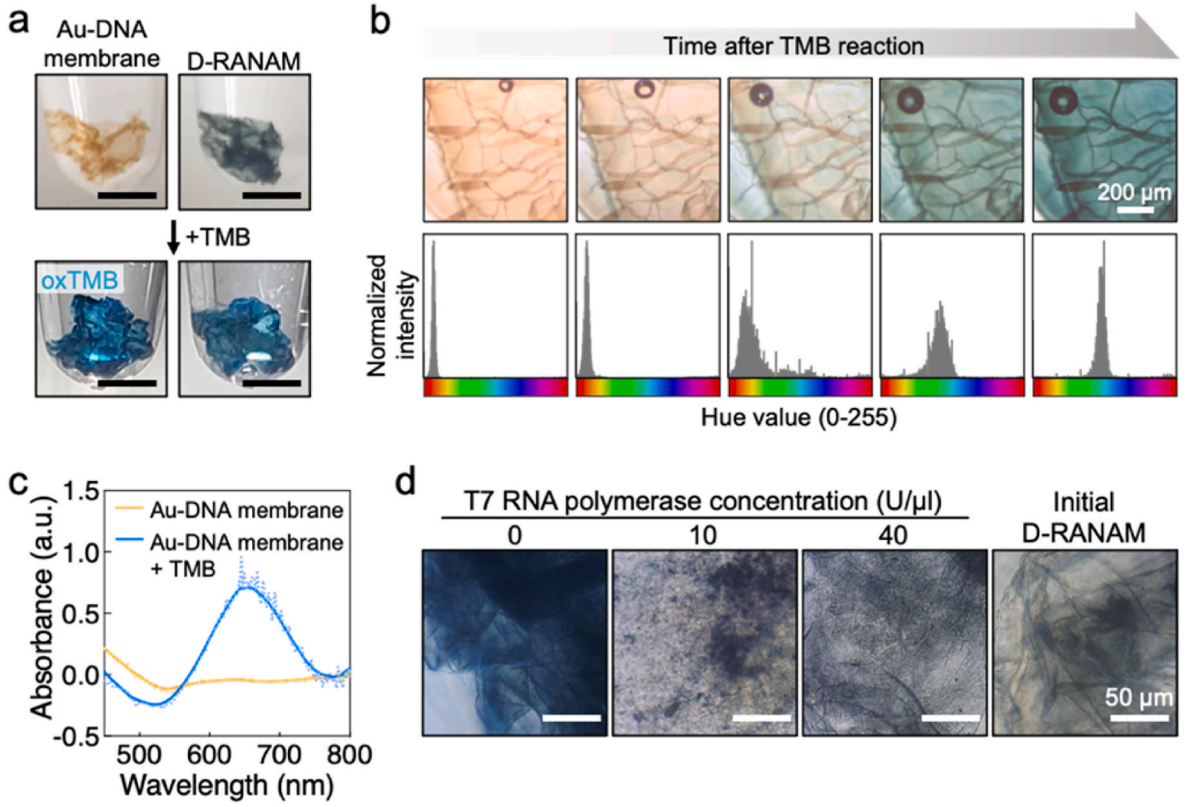

Fig. 3. Redox reaction with TMB and reduced reactivity by RNA polymerization. **(a)** Digital images of Au-DNA membrane and D-RANAM before and after the redox reaction with TMB, showing the deposit of blue oxTMB. Scale bars represent 2 mm. **(b)** Time-course colorimetric changes of Au-DNA membrane reacting with TMB for 1 h. The RGB images were converted into HSB images and the hue value of each image was quantified. **(c)** Absorbance spectra of Au-DNA membrane with or without treatment with TMB. Following the reaction with TMB, a strong absorbance was observed at 670 nm, which is the specific wavelength for oxTMB absorption. **(d)** The TMB-mediated redox reaction in the presence of different concentrations of T7 RNA polymerase. Newly generated RNA transcripts inhibited the redox reaction as the concentration of T7 RNA polymerase increased. (For interpretation of the references to color in this figure legend, the reader is referred to the Web version of this article.)

choose as the target molecule for RNA virus detection with our RNA-based RANAM. Because RNA strands of RANAM can provide a number of 3′ end sites, it is beneficial for priming RNA-initiated RNA transcription by RdRP, that is an essential catalytic protein of COVID-19 (Fig. 4a). If the RdRP was included in the testing sample, the newly generated RNA shielded the R-RANAM and blocked the redox reaction between the Au component and the TMB substrate and consequently reduced the blue coloration of R-RANAM (Fig. 4a). Indeed, the blue coloration of R-RANAM was successfully reduced in the presence of RdRP, with the reduction increasing with transcription time (Fig. 4b). Additional analysis of absorbance clearly demonstrated gradual reduction in the peak height at 670 nm in response to longer transcription times (Fig. 4c). Even 10 min of transcription lowered the color intensity by as much as half of the R-RANAM. This could be due to the RdRP-mediated cascade reaction, with the 3′ ends of newly generated RNA acting as additional templates. The blue coloration decreased significantly after 2 h of reaction, with RdRP having a color similar to that of the original R-RANAM, indicating that Au^{3+} and AuNP were efficiently covered by RNA newly produced by RdRP.

To demonstrate RdRP-driven RNA amplification on R-RANAM, SYBR green I, a NA intercalating dye, was used to stain the RNA on R-RANAMs. Significant fluorescent signal amplification was confirmed when R-RANAM reacted with RdRP (Fig. 4d). The profile of the quantified fluorescence also verified the increased intensity compared with that of R-RANAM without RdRP, indicating that RdRP successfully replicated the RNA under membrane-templated conditions. After the RdRP-mediated reaction, flower-like RNA structures were formed and expanded to cover the smooth R-RANAM surface (Fig. 4e). Taken together, the newly produced RNA bump structure hindered to exposure Au^{3+} and AuNP to TMB, supporting the blue color formation. Interestingly, the Au-RNA membrane without additional reduction failed to inhibit the TMB redox reaction even after incubation with different concentrations of RdRP, up to 100 nM (Fig. S7). These results provide evidence that Au^{3+} reduction is pivotal in exposing the 3′-ends of RNA, allowing the recognition and amplification of RNA transcripts by RdRP. Owing to the residual AuNPs, R-RANAM scaffolds also exhibited characteristic Raman spectrum of RNA compared to the initial RNA membrane (Fig. S8) (Wilson et al., 2020; Camp Jr and Cicerone, 2015; Morla-Folch et al., 2016). In the presence of RdRP, the Raman peaks of RNA were significantly enhanced due to the RdRP-directed mass production of RNA strands at the surface of R-RANAM. The result demonstrates that our R-RANAM platform would be also applied as a label-free Raman-based biosensor to detect RdRP.

3.4. Concentration-dependent RdRP detection using design-free R-RANAM biosensor

To further investigate the RdRP detection limit of the R-RANAM biosensor, the membrane was treated with various concentrations of RdRP. Blue coloration decreased gradually with increasing RdRP concentration, from 10^2 to 10^8 aM, suggesting that the tightly entangled RNA bump can successfully cover the Au component on the membrane (Fig. 5a). Compared with the initial R-RANAM, absorbance at 670 nm was significantly reduced in the case of RdRP-treated R-RANAM (Fig. 5b). Even 100 aM of RdRP could significantly mitigate the coloration compared with the control group, suggesting high sensitivity of the

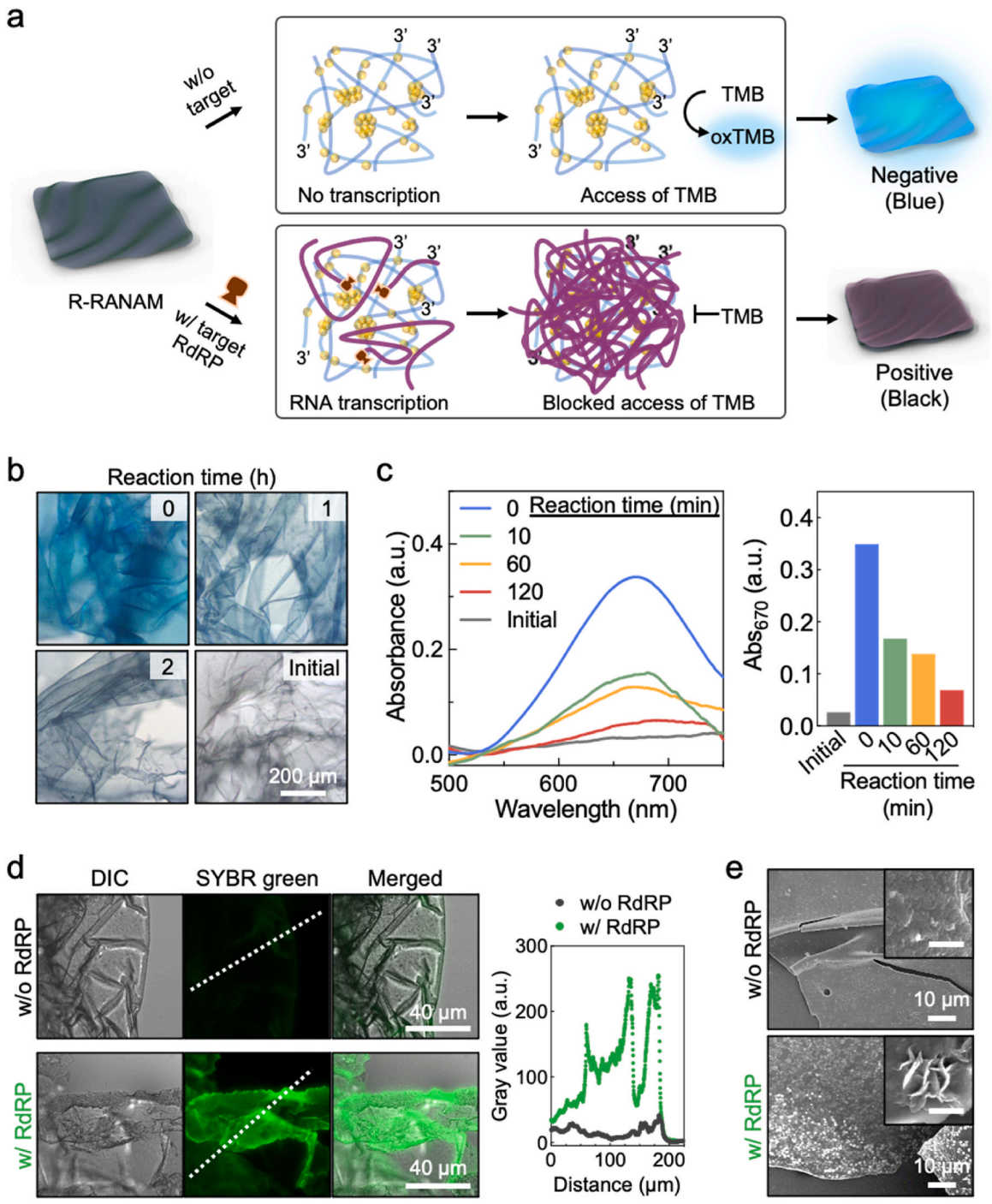

Fig. 4. R-RANAM biosensor for RdRP detection. **(a)** Schematic illustration showing the RdRP detection platform by RdRP-mediated RNA amplification to inhibition of the redox reaction. **(b)** Digital images of R-RANAMs showing that the TMB-mediated redox reaction was inhibited by increasing RdRP transcription reaction time. **(c)** Absorbance spectra of TMB-treated R-RANAMs incubated with RdRP for different durations. Absorption at oxTMB-specific wavelength reduced as the reaction time increased. **(d)** Fluorescence microscopy images of R-RANAMs stained with SYBR green I dye after 2 h incubation with or without RdRP. Newly produced RNA transcripts were visibly stained with the RNA staining dye. **(e)** FE-SEM images of R-RANAMs after reaction with or without RdRP, demonstrating the generation of flower-like RNA particles on the surface. Inset scale bars represent 500 nm. (For interpretation of the references to color in this figure legend, the reader is referred to the Web version of this article.)

R-RANAM biosensor (Fig. 5c). This means that RANAM-based detection system can achieve the sensitive detection of RdRP as low as 600 copies. Considering rapid virus growth, 100 aM of RdRP equals to the ~600 copies which indicated that RdRP-based detection is sensitive enough when compared to RNA gene-specific detection system.

Furthermore, short-term incubation with RdRP was also tested and concentration-dependent signal decrease was confirmed (Fig. S9). This indicates that longer incubation time dramatically improves the sensitivity even at low RdRP concentration. This sensitivity is comparable enough to RNA gene-specific detection system for precise diagnosis of viral infection. Further investigation by staining with SYBR green I dye showed that the green fluorescence from RdRP-treated R-RANAM was significantly higher than that from the initial R-RANAM, indicating that RNA replication was efficiently achieved (Fig. 5d). This result suggests

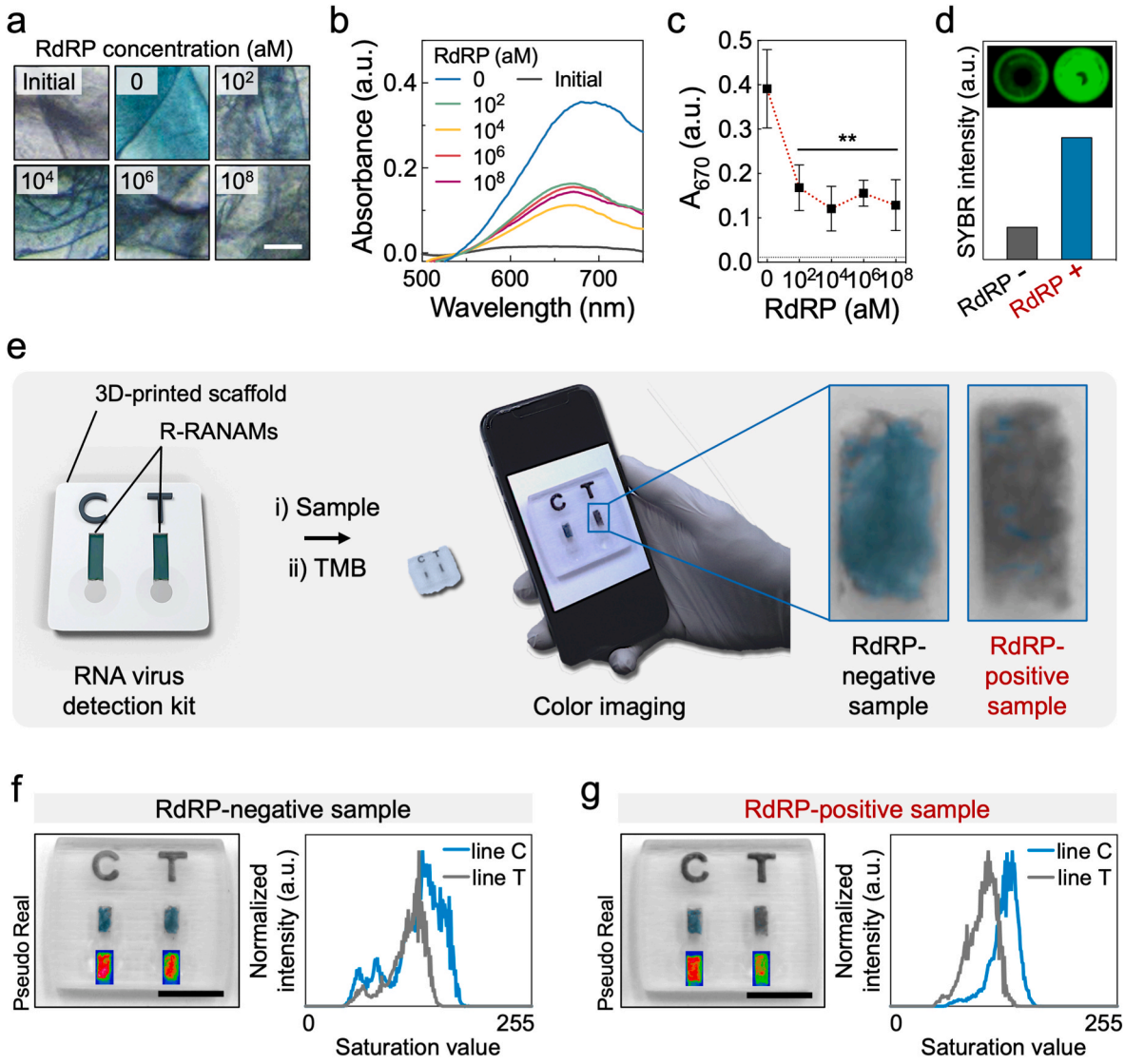

Fig. 5. Detection of viral RdRP based on the R-RANAM-based prototype kit. **(a–c)** Digital images **(a)**, absorbance spectra **(b)** and absorbance at 670 nm **(c)** of R-RANAMs incubated with the indicated concentrations of RdRP following TMB treatment. RdRP was still detectable by the R-RANAM biosensor even at minimum concentration (100 aM). Black dotted line indicates the absorbance of initial R-RANAM in **(c)**. $^{**}p < 0.01$ (one-way ANOVA followed by Tukey test, $n = 3$), compared to 0 aM RdRP-treated group. **(d)** Fluorescence images showing SYBR green I-staining of initial R-RANAM (RdRP -) or 100 pM RdRP-treated R-RANAM (RdRP +). **(e)** Illustration of the detection of RdRP using a smartphone-assisted prototype kit assembled using a 3D-printed scaffold and R-RANAMs. **(f, g)** Smartphone-assisted color imaging of prototype kit results of RdRP-negative **(f)** or RdRP-positive **(g)** testing samples. Further examination by pseudocolor and color analysis also clearly showed the viral RdRP diagnostic ability. The scale bars in **(f)** and **(g)** represent 5 mm. (For interpretation of the references to color in this figure legend, the reader is referred to the Web version of this article.)

that fluorescence analysis can also be utilized in RdRP detection with experimental equipment, indicating that the double-check system is capable of R-RANAM for precise viral detection. Moreover, the R-RANAM biosensor was independent to specific RNA sequences in the RNA membrane (Fig. S10). Taken together, R-RANAM can provide a design-free biosensor that may be widely applicable in the detection of various RNA viruses.

3.5. Smartphone-assisted RdRP-detectable prototype kit for virus detection

Based on the naked eye-detectable advantage of the R-RANAM biosensor, we devised an easy-to-use viral diagnostic prototype kit (Fig. 5e). The prototype kit was fabricated using a 3D-printed scaffold bearing the control (C) and test (T) lines embedded with two R-RANAMs. By placing the sample and the reaction mixture on the T line and TMB on both lines, the presence of viral RdRP could be confirmed based on the number of blue lines. Furthermore, universally useable smartphone camera-based color imaging supported the precise recognition of the colors of the lines in the diagnostic kit. In the absence of RdRP, two blue lines were displayed from both the C and T lines, indicating that Au components were successfully exposed to react with TMB (Fig. 5f). On the other hand, one blue line was displayed from the RdRP-positive sample solution-treated kit, indicating viral infection (Fig. 5g and Fig. S11). It is worth to note that our detection system is independent on the sequence, suggesting that our system also applicable to detect mutations of SARS-CoV-2. In addition, the pseudo-color effect made the results visible, facilitating the distinction of colors between the C and T lines. Quantification of saturation values from the HSB images further demonstrated the similarity of the colors between the C and T lines from digital images, which also demonstrated the clearly distinct intensity. Meanwhile, the R-RANAM maintained its at least 20 days at

room temperature, suggesting that R-RANAM is stable enough for the storage as a pre-loaded kit which makes convenient for practical application intact (Fig. S12). These results imply that the R-RANAM biosensor has great potential as a simple and self-diagnostic smartphone-assisted viral detection kit.

4. Conclusions

In this study, we proposed a RANAM biosensor for a novel RNA virus detection with RNA polymerase activity. In the presence of RNA polymerase, RANAM-templated RNA transcription led to coverage of the Au component by the newly generated RNA bump, sequentially decreasing the coloration via the oxidation of TMB. As a proof of concept, R-RANAM was utilized as a biosensor for detecting RdRP, which can be produced by viral genes, in RNA viruses. Due to the efficient RNA-directed RNA transcription of RdRP on R-RANAM, the presence of RdRP was clearly observed with the naked eye based on a decrease in the blue coloration, which occurred even at 100 aM of RdRP. To demonstrate practical application of the R-RANAM biosensor, we developed an easy-to-use and self-operating diagnostic prototype kit with R-RANAM. Using smartphone-supported color imaging, the RdRP-dependent coloration of the C and T lines could be confirmed simply and clearly. Taken together, this study shows that the R-RANAM biosensor has the potential to facilitate easy diagnosis of viral infections without requiring any highly trained personnel or expensive equipment. We expect that this RdRP-detectable biosensor will not only be applicable for detection of variant of RNA viruses, but will also provide a facile POCT platform for rapid, sensitive, and simple detection of emerging viruses such as SARS-CoV-2.

Credit authorship contribution statement

Dajeong Kim: Investigation, Conceptualization, Writing – original draft. Sangwoo Han: Investigation, Conceptualization, Writing – original draft. Yoonbin Ji: Visualization, Investigation. Heejeong Youn: Resources, Investigation. Hyejin Kim: Investigation. Ohsung Ko: Investigation. Jong Bum Lee: Supervision, Conceptualization, Writing – review & editing.

Declaration of competing interest

The authors declare that they have no known competing financial interests or personal relationships that could have appeared to influence the work reported in this paper.

Acknowledgement

This work was supported by the Creative Materials Discovery Program through the National Research Foundation of Korea (NRF) funded by the Ministry of Science and ICT (MSIT) (NRF-2017M3D1A1039423), the Commercialization Promotion Agency for R&D Outcomes (COMPA) funded by the MSIT (2021-RMD-S04), and the NRF funded by the MSIT (NRF-2017R1E1A1A01075027).

Appendix A. Supplementary data

Supplementary data to this article can be found online at https://doi.org/10.1016/j.bios.2021.113880.

References

Abi, A., Mohammadpour, Z., Zuo, X., Safavi, A., 2018. Biosens. Bioelectron. 102, 479–489.
Aftab, S.O., Ghouri, M.Z., Masood, M.U., Haider, Z., Khan, Z., Ahmad, A., Munawar, N., 2020. J. Transl. Med. 18, 275.
Ahlquist, P., 2002. Science 296, 1270–1273.
Ai, T., Yang, Z., Hou, H., Zhan, C., Chen, C., Lv, W., Tao, Q., Sun, Z., Xia, L., 2020. Radiology 296, E32–E40.
Ascoli, C.A., 2021. Nat. Biotechnol. 39, 274–275.
Berti, L., Burley, G.A., 2008. Nat. Nanotechnol. 3, 81–87.
Camp Jr., C.H., Cicerone, M.T., 2015. Nat. Photonics 9, 295–305.
Carter, L.J., Garner, L.V., Smoot, J.W., Li, Y., Zhou, Q., Saveson, C.J., Sasso, J.M., Gregg, A.C., Soares, D.J., Beskid, T.R., Jervey, S.R., Liu, C., 2020. ACS Cent. Sci. 6, 591–605.
Che, Y., Zinchenko, A., Murata, S., 2015. J. Colloid Interface Sci. 445, 364–370.
Chen, M., Lu, R., Yu, A., 2020. Mater. Lett. 263, 127253.
Chen, Z., Liu, C., Cao, F., Ren, J., Qu, X., 2018. Chem. Soc. Rev. 47, 4017–4072.
Corman, V.M., Landt, O., Kaiser, M., Molenkamp, R., Meijer, A., Chu, D.K., Bleicker, T., Brunink, S., Schneider, J., Schmidt, M.L., Mulders, D.G., Haagmans, B.L., van der Veer, B., van den Brink, S., Wijsman, L., Goderski, G., Romette, J.L., Ellis, J., Zambon, M., Peiris, M., Goossens, H., Reusken, C., Koopmans, M.P., Drosten, C., 2020. Euro Surveill. 25.
Du, Y., Dong, S., 2017. Anal. Chem. 89, 189–215.
Dulin, D., Vilfan, I.D., Berghuis, B.A., Poranen, M.M., Depken, M., Dekker, N.H., 2015. Nucleic Acids Res. 43, 10421–10429.
Ejazi, S.A., Ghosh, S., Ali, N., 2021. Immunol. Cell Biol. 99, 21–33.
Fang, Y., Zhang, H., Xie, J., Lin, M., Ying, L., Pang, P., Ji, W., 2020. Radiology 296, E115–E117.
Ferrero, D.S., Buxaderas, M., Rodriguez, J.F., Verdaguer, N., 2015. PLoS Pathog. 11, e1005265.
Han, D., Park, Y., Kim, H., Lee, J.B., 2014. Nat. Commun. 5, 4367.
Han, S., Ko, O., Lee, G., Jeong, S.W., Choi, Y.J., Lee, J.B., 2021. Nano Lett. 21, 462–468.
Ji, T., Liu, Z., Wang, G., Guo, X., Akbar Khan, S., Lai, C., Chen, H., Huang, S., Xia, S., Chen, B., Jia, H., Chen, Y., Zhou, Q., 2020. Biosens. Bioelectron. 166, 112455.
Kevadiya, B.D., Machhi, J., Herskovitz, J., Oleynikov, M.D., Blomberg, W.R., Bajwa, N., Soni, D., Das, S., Hasan, M., Patel, M., Senan, A.M., Gorantla, S., McMillan, J., Edagwa, B., Eisenberg, R., Gurumurthy, C.B., Reid, S.P.M., Punyadeera, C., Chang, L., Gendelman, H.E., 2021. Nat. Mater. 20, 593–605.
Kim, D., Kim, J., Lee, J.B., 2020. Chem. Commun. 56, 5917–5920.
Krishnan, Y., Simmel, F.C., 2011. Angew Chem. Int. Ed. Engl. 50, 3124–3156.
Kunoh, T., Takeda, M., Matsumoto, S., Suzuki, I., Takano, M., Kunoh, H., Takada, J., 2018. ACS Sustain. Chem. Eng. 6, 364–373.
Lee, C.Y., Lin, R.T.P., Renia, L., Ng, L.F.P., 2020. Front. Immunol. 11, 879.
Lee, W.K., Kwon, K., Choi, Y., Lee, J.S., 2021. J. Colloid Interface Sci. 594, 160–172.
Li, X., Gao, L., Chen, Z., 2019. Spectrochim. Acta Mol. Biomol. Spectrosc. 213, 37–41.
Ma, X., Song, S., Kim, S., Kwon, M.S., Lee, H., Park, W., Sim, S.J., 2019. Nat. Commun. 10, 836.
Machitani, M., Yasukawa, M., Nakashima, J., Furuichi, Y., Masutomi, K., 2020. Cancer Sci. 111, 3976–3984.
Morla-Folch, J., Xie, H.N., Alvarez-Puebla, R.A., Guerrini, L., 2016. ACS Nano 10, 2834–2842.
Picarazzi, F., Vicenti, I., Saladini, F., Zazzi, M., Mori, M., 2020. Molecules 25.
Pokhrel, R., Chapagain, P., Siltberg-Liberles, J., 2020. J. Med. Microbiol. 69, 864–873.
Qing, Z., Bai, A., Xing, S., Zou, Z., He, X., Wang, K., Yang, R., 2019. Biosens. Bioelectron. 137, 96–109.
Song, Q., Sun, X., Dai, Z., Gao, Y., Gong, X., Zhou, B., Wu, J., Wen, W., 2021. Lab Chip 21, 1634–1660.
Wang, X., Yang, Y., Li, L., Sun, M., Yin, H., Qin, W., 2014. Anal. Chem. 86, 4416–4422.
Wilson, A.L., Outeiral, C., Dowd, S.E., Doig, A.J., Popelier, P.L., Waltho, J.P., Almond, A., 2020. Commun. Chem. 3, 1–9.
Wu, L., Wang, J., Ren, J., Qu, X., 2014. Adv. Funct. Mater. 24, 2727–2733.
Xia, X., Zhang, J., Sawall, T., 2015. Anal. Methods 7, 3671–3675.
Zhou, L., Ren, J., Qu, X., 2017. Mater. Today 20, 179–190.
Zinchenko, A., Che, Y., Taniguchi, S., Lopatina, L.I., Sergeyev, V.G., Murata, S., 2016. J. Nanopart. Res. 18, 1–9.
Zuber, A., Purdey, M., Schartner, E., Forbes, C., Van der Hoek, B., Giles, D., Abell, A., Monro, T., Ebendorff-Heidepriem, H., 2016. Sensor. Actuator. B Chem. 227, 117–127.